Available online at www.sciencedirect.com
ScienceDirect
Trans. Nonferrous Met. Soc. China 34(2024) 2167−2180
Transactions of Nonferrous Metals Society of China
www.tnmsc.cn

Corrosion behavior of Ti−6Al−4V alloy fabricated by selective laser melting in simulated spent fuel reprocessing environment

Zheng LIU[1,2], Lian-min ZHANG[1], De-chun REN[3], Ai-li MA[1], Hai-bin JI[3], Yu-gui ZHENG[1]

1. CAS Key Laboratory of Nuclear Materials and Safety Assessment, Institute of Metal Research, Chinese Academy of Sciences, Shenyang 110016, China;
2. School of Materials Science and Engineering, University of Science and Technology of China, Shenyang 110016, China;
3. Shi-changxu Innovation Center for Advanced Materials, Institute of Metal Research, Chinese Academy of Sciences, Shenyang 110016, China

Received 18 January 2023; accepted 19 July 2023

Abstract: The corrosion behavior of Ti−6Al−4V fabricated by selective laser melting (SLM) in simulated spent fuel reprocessing environment was investigated. The microstructure and corrosion resistance of SLM Ti−6Al−4V alloy were characterized by optical microscopy, X-ray diffraction, scanning electron microscopy, electron backscatter diffraction and electrochemical tests. It can be found that SLM Ti−6Al−4V alloy has a better corrosion resistance than the cast counterpart in 6 mol/L hot nitric acid with oxidizing ions. Further analysis indicates that SLM Ti−6Al−4V alloy exhibits $\alpha'+\beta$ microstructure with smaller grain size and higher grain boundary density in comparison to the cast counterpart, and a higher β-Ti phase content with uniform distribution is also observed in SLM alloy, which is conducive to enhancing its passivation ability in nitric acid with oxidizing ions, contributing to an improved corrosion resistance. It is indicated that SLM Ti−6Al−4V alloy has the potential to be used in spent fuel reprocessing process.

Key words: spent fuel reprocessing; selective laser melting; Ti−6Al−4V alloy; corrosion behavior; passivation ability

1 Introduction

Spent fuel reprocessing refers to the chemical process through high-temperature nitric acid to dissolve spent fuel [1,2]. The nitric acid media containing a large amount of dissolved species such as oxidizing Ce^{4+}, Cr^{6+} and Pu^{4+} can be strongly corrosive towards structural materials. Austenitic stainless steels with a low carbon content are extensively used as the structural materials in spent fuel reprocessing due to possessing good corrosion resistance and low cost [3−5]. However, under extremely harsh corrosive environment of high temperature and concentrated nitric acid with oxidizing ions, stainless steels are subjected to severe intergranular corrosion (IGC), which can bring potential safety hazard to spent fuel reprocessing plants [6,7]. Unlike stainless steels, titanium alloys do not encounter IGC in reprocessing environment due to their inherently high corrosion resistance. Accordingly, titanium alloys have been the choice of materials for some critical equipment, e.g., dissolver and evaporator, in reprocessing plants [8,9]. However, due to the poor fabricability of titanium alloys, it is difficult to manufacture fine and complex customized parts efficiently, which has become a bottleneck in the

Corresponding author: Lian-min ZHANG, Tel: +86-24-23915904, E-mail: lmzhang14s@imr.ac.cn;
Yu-gui ZHENG, Tel: +86-24-23928381, E-mail: ygzheng@imr.ac.cn
DOI: 10.1016/S1003-6326(24)66532-5

further application of titanium alloys in the reprocessing plants.

Fortunately, emerging additive manufacturing (AM) technology provides an admirable approach to solve the fabricability problem of titanium alloys since AM enables to produce diverse metal parts with complex configuration and high precision at relatively low cost [10−12]. As one of the important AM technologies, selective laser melting (SLM), which uses the computer-based laser beam to build the parts layer by layer through melting and consolidating the powder, is extensively employed to fabricate various key components in biomedical, aerospace and nuclear power fields [12−14]. By adjusting the fabrication parameters of SLM, the mechanical properties of SLM titanium alloys can approach or even surpass those of the traditional titanium alloys [15−17]. For instance, the biomedical Ti−24Nb−4Zr−8Sn alloy produced by SLM showed similar mechanical properties to the alloy with traditional processing methods [18]. Meanwhile, the SLM pure titanium displayed a better wear resistance in comparison to the cast counterpart [16,19]. The superiority in mechanical properties of SLM titanium alloys is mainly attributed to their unique microstructure. Due to the layered manufacturing characteristics of SLM technology, the rapid melting and solidification of powder promote the formation of fine microstructures, which is beneficial to the improvement in mechanical properties of SLM titanium alloys [20,21]. However, compared with the widely studied mechanical properties, the corrosion resistance of SLM titanium alloys has only been investigated recently [22,23]. It is well accepted that the special microstructure of SLM titanium alloys will result in different corrosion behavior compared with traditionally processed titanium alloys, and the subsequent heat treatment of SLM titanium alloys will significantly improve the corrosion resistance [23,24]. Consequently, due to the characteristics of SLM technology and the satisfactory comprehensive properties of SLM titanium alloys, SLM titanium alloys are widely applied in various fields and can be extremely promising structure materials in spent fuel reprocessing. Yet, to the best of the authors' knowledge, the research on the corrosion behavior of SLM titanium alloys in the simulating environment of spent fuel reprocessing, which can contribute to a comprehensive and in-depth understanding of the corrosion mechanism of SLM alloy and promote its application in spent fuel reprocessing, is lacking.

Herein, the corrosion behavior of SLM Ti−6Al−4V alloy and the cast counterpart in 6 mol/L hot nitric acid with oxidizing ions was investigated. Microstructure, corrosion morphology and passive film characteristics of both SLM Ti−6Al−4V alloy and the cast counterpart were characterized by various methods. This work can provide an important insight for the material manufacturing of reprocessing equipment and reveal the corrosion mechanism of SLM alloys in spent fuel reprocessing.

2 Experimental

2.1 Materials and sample preparation

SLM Ti−6Al−4V alloy and the cast counterpart were used in this work, and their chemical composition is listed in Table 1. SLM Ti−6Al−4V alloy was produced by Concept Laser M2 machine in high purity Ar atmosphere. Small rods with a diameter of 12 mm and a length of 60 mm were manufactured using laser power of 370 W, laser energy density of 208 J/mm^3 and laser scan speed of 1500 mm/s. The specially prepared T-shape samples were cut for the electrochemical measurements, where the front part was cuboid with a size of 8 mm × 8 mm × 3 mm, and the rear part was a cylinder with a diameter of 3 mm and a length of 10 mm. It should be pointed out that a Teflon sleeve was heated to seal the rear part of the samples before the electrochemical measurements. Samples with a dimension of 5 mm × 5 mm × 2 mm were cut for mass loss tests. Prior to experimental measurements, all the samples were wet ground

Table 1 Chemical composition of SLM Ti−6Al−4V alloy and cast counterpart (wt.%)

Sample	C	H	O	N	Fe	Al	V	Ti
SLM Ti−6Al−4V	0.017	0.002	0.12	0.02	0.16	5.89	4.06	Bal.
Cast counterpart	0.025	0.002	0.14	0.05	0.36	6.02	4.08	Bal.

with SiC emery paper up to 2000 grit size. Afterward, all the samples were ultrasonically cleaned with deionized water and ethanol, respectively, and then dried by cold wind using a blower.

2.2 Microstructural characterization

The microstructure of SLM Ti−6Al−4V alloy and the cast counterpart was observed by using optical microscopy (OM, Observer Z1m, Zeiss, Germany), scanning electron microscopy (SEM, Inspect F50, FEI, USA) and electron backscatter diffraction (EBSD, Quattro S, Thermo Scientific, USA). The samples used for OM and SEM were polished to 2000 grit using SiC paper, then etched in a Kroll's solution, and finally cleaned in ethanol and deionized water by ultrasound. Afterwards, the samples for EBSD were wet ground with SiC paper up to 5000 grit, followed by vibration polishing to remove the surface stress. Furthermore, the microstructural constituents of the samples were investigated by means of X-ray diffraction (XRD, Bruker, Karlsruhe, Germany).

2.3 Electrochemical measurements

High-temperature nitric acid electrochemical measurements were conducted at 95 °C in a glass cell with a three-electrode configuration using an electrochemical workstation (Reference 600+, Gamry Instruments, Inc. USA), as shown in Fig. 1. Ti−6Al−4V samples, platinum sheet and saturated calomel electrode (SCE) corresponded to working electrode, counter electrode and reference electrode, respectively. The experiment electrolyte was 6 mol/L nitric acid containing Cr^{6+}, Ce^{4+} and V^{5+} (the corresponding additives were CrO_3, metallic V and $Ce(NH_4)_2(NO_3)_6$, respectively) to simulate the environment of spent fuel reprocessing. The solution preparation principle and the specific composition of the solution could be referred to our previous work [25].

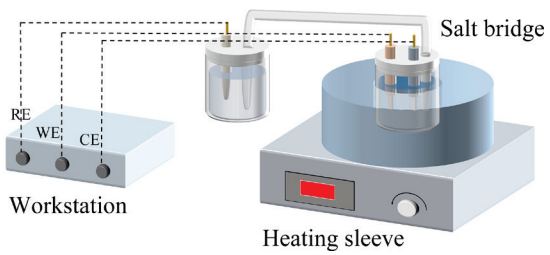

Fig. 1 High-temperature nitric acid electrochemical measurement apparatus (RE−Reference electrode; WE−Working electrode; CE−Counter electrode)

Before electrochemical tests, the working electrode was immersed into experiment solution at 95 °C for 24 h to approximate the stable potential in nitric acid. Electrochemical impedance spectroscopy (EIS) measurements were carried out in the frequency range from 100 kHz to 0.1 Hz at OCP. Potentiodynamic polarization measurements were carried out from −500 mV (vs OCP) to 2200 mV (vs SCE) at a scanning rate of 0.5 mV/s. The potentiostatic polarization measurements were performed at a potential of 1300 mV (vs SCE), and the response of the current versus time was recorded. Moreover, Mott−Schottky measurements were conducted at a frequency of 1000 Hz with a scanning rate of 20 mV/s. And the initial potential of Mott−Schottky measurements was −500 mV (vs OCP), while the final potential was +2000 mV (vs OCP). All electrochemical measurements were conducted three times to ensure the reproducibility.

2.4 Mass loss measurements

Samples of SLM Ti−6Al−4V alloy and the cast counterpart were immersed in 6 mol/L nitric acid with oxidizing ions at 95 °C for 120 h, and the corrosion mass loss was measured for each sample in order to compare the corrosion resistance of these two titanium alloys. The corrosion rate was determined by using equation as follows:

$$V_{corr}=8.76\times10^{4}W/(StD) \quad (1)$$

where V_{corr} is corrosion rate (mm/a), t is the time of immersion (h), S is the total surface area of samples (cm^2), W is mass loss (g), and D is the density of samples (g/cm^3). Additionally, the corrosion morphologies of SLM Ti−6Al−4V alloy and the cast counterpart after immersing were observed by SEM.

2.5 Surface analysis

The samples with a dimension of 5 mm × 5 mm × 2 mm after immersing in 6 mol/L hot nitric acid containing oxidizing ions for 48 h were rinsed with deionized water and ethanol, and then dried with cold wind. Subsequently, X-ray photoelectron spectroscopy (XPS, ESCALAB250, Waltham, USA) tests were conducted immediately to avoid the oxidation of air. High-resolution spectra of Ti 2p, Al 2p and V 2p were obtained at a pass energy of 50 eV with an energy step size of 0.1 eV. The binding energy was calibrated by C 1s with the

standard value of 284.6 eV. XPSPEAK 4.1 software was used to fit those spectra, where the commonly used Gaussian−Lorentzian mix function and Shirley background subtraction were applied.

3 Results

3.1 Microstructure and phase composition

Figure 2 shows the microstructure of SLM Ti−6Al−4V alloy and the cast counterpart. For SLM Ti−6Al−4V alloy, a fine acicular α' martensitic microstructure which is produced by the rapid melting and solidification of powder during SLM fabricating process is observed, as shown in Fig. 2(a) [20,26]. In addition, prior columnar β grains with remarkable layer boundaries are observed in Fig. 2(c). The existence of prior β grains is mainly attributed to the absence of the

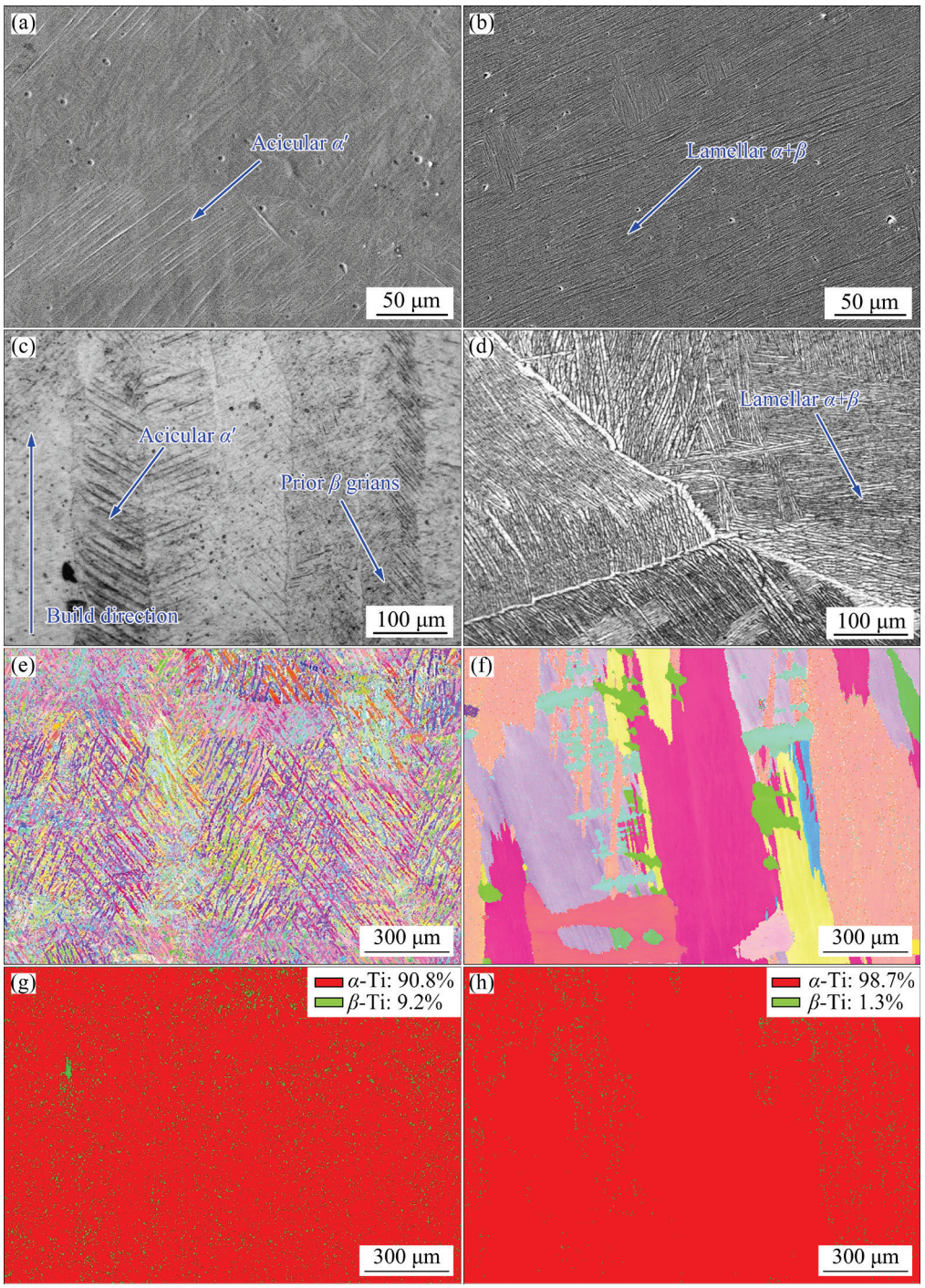

Fig. 2 SEM images (a, b), OM images (c, d), IPF maps of EBSD (e, f), and phase maps of EBSD (g, h) for SLM Ti−6Al−4V alloy (a, c, e, g) and cast counterpart (b, d, f, h)

nucleation barrier during the SLM solidification process [27]. However, for the cast counterpart, Figs. 2(b, d) indicate a lamellar α+β microstructure. It should be pointed out that the grain size of the cast counterpart is larger than that of SLM Ti−6Al−4V alloy. To better investigate the microstructure of SLM Ti−6Al−4V alloy and the cast counterpart, EBSD measurements are conducted. Figures 2(e, f) show the IPF map for SLM alloy and the cast counterpart. Obviously, SLM alloy displays a fine microstructure with the small grain size, while the cast counterpart presents a large grain size. Moreover, a uniform distribution and a selective distribution of β-Ti phase are recorded in SLM alloy and the cast counterpart, respectively, as shown in Figs. 2(g, h). Furthermore, the contents of α-Ti (α'-Ti) and β-Ti in both SLM Ti−6Al−4V alloy and the cast counterpart are obtained from the phase map, which are 90.8% and 9.2% for the SLM Ti−6Al−4V alloy, and 98.7% and 1.3% for the cast counterpart, respectively.

Figure 3 displays the XRD patterns of SLM Ti−6Al−4V alloy and the cast counterpart. It can be seen that, for these two titanium alloys, the main peaks in XRD pattern belong to α-Ti (α'-Ti) phase, while weak peaks of β-Ti phase are also observed in XRD pattern. According to literature, the peak near 2θ=39.5° is considered to be β-Ti phase [28], while the peak near 2θ=72° also represents β-Ti [29]. Based on the XRD patterns, the volume fraction of α-Ti (α'-Ti) and β-Ti are calculated, which are 90.4% and 9.6% for SLM Ti−6Al−4V alloy, and 97.6% and 2.4% for the cast counterpart, as given in Table 2 [30,31]. Obviously, SLM Ti−6Al−4V alloy has a higher content of β-Ti phase, which is consistent with the results obtained by EBSD results.

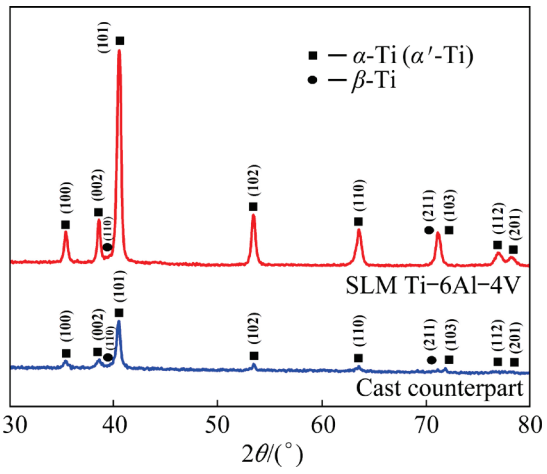

Fig. 3 XRD patterns of SLM Ti−6Al−4V alloy and cast counterpart

Table 2 Phase constituents and their volume fraction (V_f) of SLM Ti−6Al−4V alloy and cast counterpart estimated from XRD data

Sample	Phase constituent	$V_{f,\alpha}$ ($V_{f,\alpha'}$)/%	$V_{f,\beta}$/%
SLM Ti−6Al−4V	α'+β	90.4	9.6
Cast counterpart	α+β	97.6	2.4

3.2 Electrochemical properties

The electrochemical measurement results of SLM Ti−6Al−4V alloy and the cast counterpart in hot nitric acid with oxidizing ions are shown in Fig. 4. Figure 4(a) shows the variations in OCP of the SLM Ti−6Al−4V alloy and the cast counterpart. Clearly, OCP of both titanium alloys keeps the stable potential with only 2 mV potential fluctuations. The stable values of OCP for SLM Ti−6Al−4V alloy and the cast counterpart are 1067 and 1018 mV, respectively, indicating only little difference of OCP between these two alloys. Figure 4(b) shows the potentiodynamic polarization plots of the SLM Ti−6Al−4V alloy and the cast counterpart. It can be seen that the range of passive domain and the shape of cathodic plots are similar for both SLM Ti−6Al−4V alloy and the cast counterpart, suggesting a similar corrosion behavior of these two alloys. According to literatures [32,33], in nitric acid containing oxidizing ions, the anodic reaction is the dissolution of metal, while the cathodic reactions usually refer to the autocatalytic reduction of nitric acid and the reduction of oxidizing ions. Furthermore, the relevant potentiodynamic polarization parameters including φ_{corr}, corrosion current density (J_{corr}) and passive current density (J_{pass}) are given in Table 3. The J_{corr} and J_{pass} of SLM Ti−6Al−4V alloy are 8.30 and 17.15 μA/cm^2, respectively, which are lower than those of the cast counterpart. Apparently, SLM Ti−6Al−4V alloy has a better corrosion resistance than the cast counterpart. Meanwhile, the φ_{corr} is 1060 mV for SLM Ti−6Al−4V alloy, while it is 1019 mV for the cast counterpart. In addition, Fig. 4(c) presents the results of potentiostatic polarization for these two alloys. It can be found that the J_{pass} of the cast counterpart under the applied potential is higher than that of the SLM

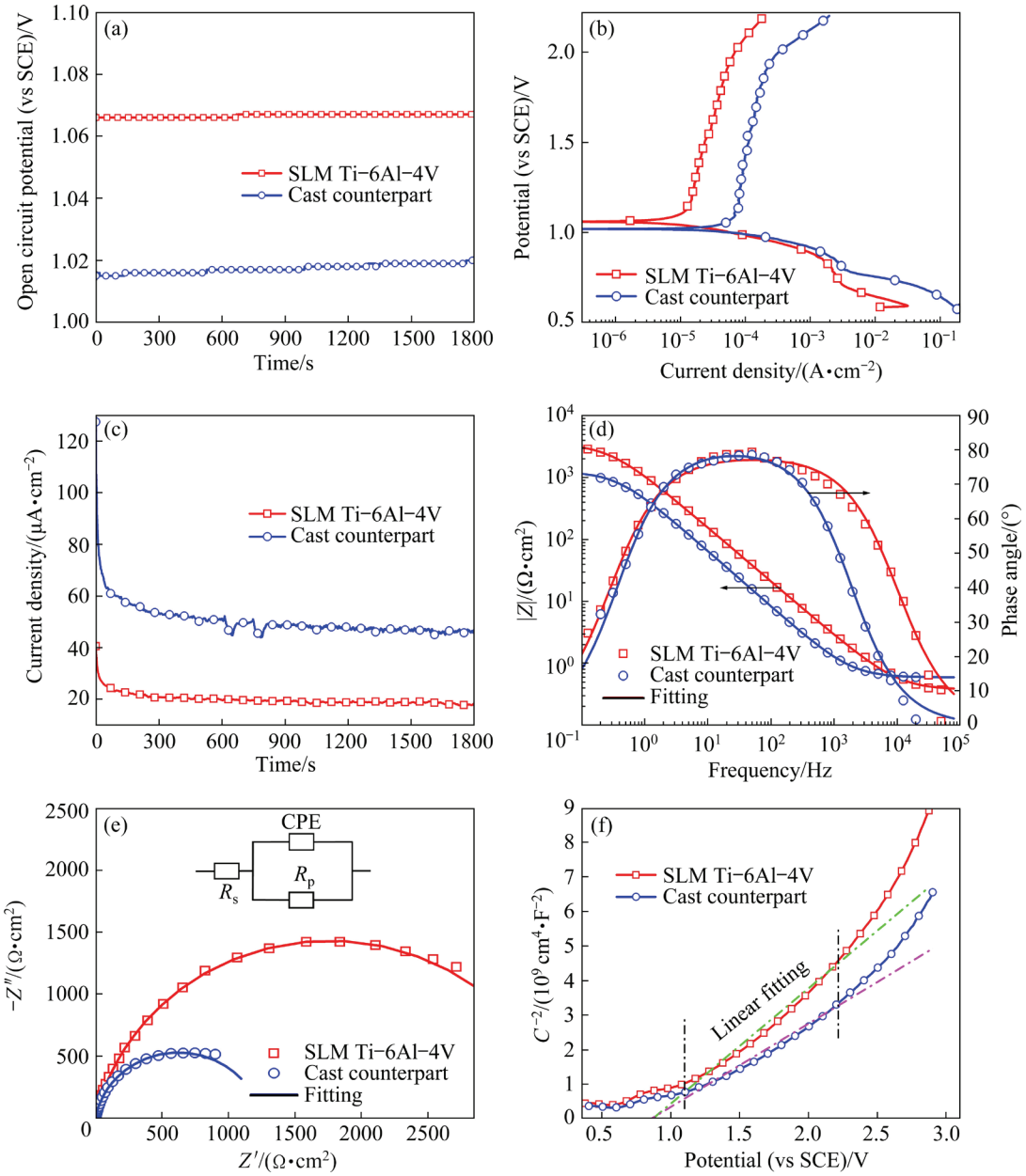

Fig. 4 Electrochemical measurement results: (a) OCP plots; (b) Potentiodynamic polarization plots; (c) Potentiostatic polarization plots; (d) Bode plots; (e) Nyquist plots; (f) Mott−Schottky plots

Table 3 Potentiodynamic polarization parameters of SLM Ti−6Al−4V alloy and cast counterpart in 6 mol/L hot nitric acid with oxidizing ions

Sample	φ_{corr}(vs SCE)/mV	J_{corr}/(μA·cm^{-2})	J_{pass}(at 1500 mV (vs SCE)/(μA·cm^{-2})
SLM Ti−6Al−4V	1060	8.30	17.15
Cast counterpart	1019	42.03	85.87

Ti−6Al−4V alloy, indicating a better passivation ability of the later. On the whole, both potentiodynamic and potentiostatic polarization results all demonstrate a better corrosion resistance of SLM alloy compared with the cast counterpart.

EIS measurements are conducted at OCPs to further analyze the corrosion behavior of these two alloys. Figures 4(d, e) show the Bode plots and Nyquist plots of SLM Ti−6Al−4V alloy and the cast counterpart, respectively. According to relevant investigations, the equivalent circuit as shown in the insert of Fig. 4(e) is used to fit the EIS data [9], and the fitting results are given in Table 4, where R_s is the solution resistance of nitric acid, R_p is the polarization resistance, CPE is the constant phase

element. χ^2 is the fitting error. The impedance expression of CPE is given by

$$Z_{\mathrm{CPE}}=1/[T'(\mathrm{j}\omega)^n] \tag{2}$$

where T' and n are frequency-independent fitting parameters, j is the imaginary number and equal to $(-1)^{1/2}$, ω is the angular frequency and equal to $2\pi f$, and f represents the frequency (Hz). It should be pointed out that R_p is regard as the limiting step of corrosion process, and it is inversely proportional to the corrosion rate and directly proportional to the corrosion resistance. As given in Table 4, a larger value of R_p of SLM Ti−6Al−4V alloy is displayed, indicating a better corrosion resistance of SLM Ti−6Al−4V alloy.

The corrosion resistance of titanium alloys in nitric acid is mainly related to the characteristics of passive film, and thus the passive film thickness of these two alloys are calculated using the EIS data according to the following formula [34]:

$$d=\frac{\varepsilon_0\varepsilon A}{C_{\mathrm{eff}}} \tag{3}$$

where d is the thickness of the passive film, ε is dielectric constant of the passive film and taken as 85 [34], ε_0 is the vacuum permittivity (8.8542×10^{-14} F/cm), A is the effective surface area, and C_{eff} is the effective capacitance.

In this study, C_{eff} can be calculated by the following formula [34,35]:

$$C_{\mathrm{eff}}=Q^{1/\alpha}R_{\mathrm{f}}^{(1-\alpha)/\alpha} \tag{4}$$

where Q is the magnitude of CPE, R_f is film resistance and can be expressed as R_p in this study, and α is dispersion coefficient. The passive film thickness (d) is given in Table 4. Clearly, the value of d for SLM Ti−6Al−4V alloy is 2.01 nm, which is larger than that (0.96 nm) of the cast counterpart.

Figure 4(f) shows the Mott−Schottky plots of passive films formed on SLM Ti−6Al−4V alloy and the cast counterpart in the nitric acid containing oxidizing ions. It can be seen that Mott−Schottky plots of both two alloys display a positive linear range within the measured potential range, indicating that the passive films of these two alloys present the characteristic of n-type semiconductor. The Mott−Schottky equation of n-type semiconductor is expressed by [36]

$$C_{\mathrm{sc}}^{-2}=\frac{2}{\varepsilon\varepsilon_0 eN_{\mathrm{D}}}\left(E-E_{\mathrm{FB}}-\frac{kT}{e}\right) \tag{5}$$

where C_{sc} is the space-charge capacitance, N_D is the donor concentration in the n-type passive film, E is the applied potential, E_{FB} is the flat-band potential, k is Boltzmann constant (1.38×10^{-23} J/K), e is electron charge (1.6×10^{-19} C) and T is the temperature (K). Therefore, the value of N_D can be calculated by linear fitting of Mott−Schottky plots according to Eqs. (6) and (7):

$$K_{\mathrm{slope}}=\frac{\mathrm{d}C^{-2}}{\mathrm{d}E}=\frac{2}{\varepsilon\varepsilon_0 eN_{\mathrm{D}}} \tag{6}$$

$$N_{\mathrm{D}}=\frac{2}{\varepsilon\varepsilon_0 eK_{\mathrm{slope}}} \tag{7}$$

Table 5 gives Mott−Schottky fitting parameters and the calculated values of N_D for SLM Ti−6Al−4V alloy and the cast counterpart. It is clear that all R^2 values are 0.98 indicating a high level of linearity. Meanwhile, the N_D is 4.98×10^{20} and 6.89×10^{20} cm^{-3} for SLM Ti−6Al−4V alloy and the cast counterpart, respectively. The conductivity of passive film is reflected by N_D, and a lower value of N_D usually means a higher film resistance implying a better protection ability of the passive film [37]. Hence, it can be inferred that SLM Ti−6Al−4V alloy has a more protective passive film compared with the cast counterpart based on the analysis of N_D.

3.3 Corrosion rate and corrosion morphology

Mass loss measurements are carried out to characterize the long-term corrosion resistance of SLM Ti−6Al−4V alloy and the cast counterpart in 6 mol/L hot HNO_3 with oxidizing ions. Figure 5(a) shows the corrosion rate of these two alloys after

Table 4 EIS fitted values of SLM Ti−6Al−4V alloy and cast counterpart in 6 mol/L hot nitric acid with oxidizing ions

Sample	R_s/(Ω·cm^2)	CPE		R_p/(Ω·cm^2)	χ^2	C_{eff}/(F·cm^{-2})	d/nm
		Q/(Ω^{-1}· s$^{-\alpha}$· cm^{-2})	α				
SLM Ti−6Al−4V	0.37	1.76×10^{-4}	0.87	3.52×10^{3}	2.84×10^{-3}	1.64×10^{-4}	2.01
Cast counterpart	0.59	3.77×10^{-4}	0.90	1.25×10^{3}	9.51×10^{-4}	3.47×10^{-4}	0.96

Table 5 Fitting parameters of Mott−Schottky plots and calculated N_D values of SLM Ti−6Al−4V alloy and cast counterpart

Sample	Slope/10^9	N_D/10^{20}cm^{-3}	R^2
SLM Ti−6Al−4V	3.34	4.98	0.98
Cast counterpart	2.41	6.89	0.98

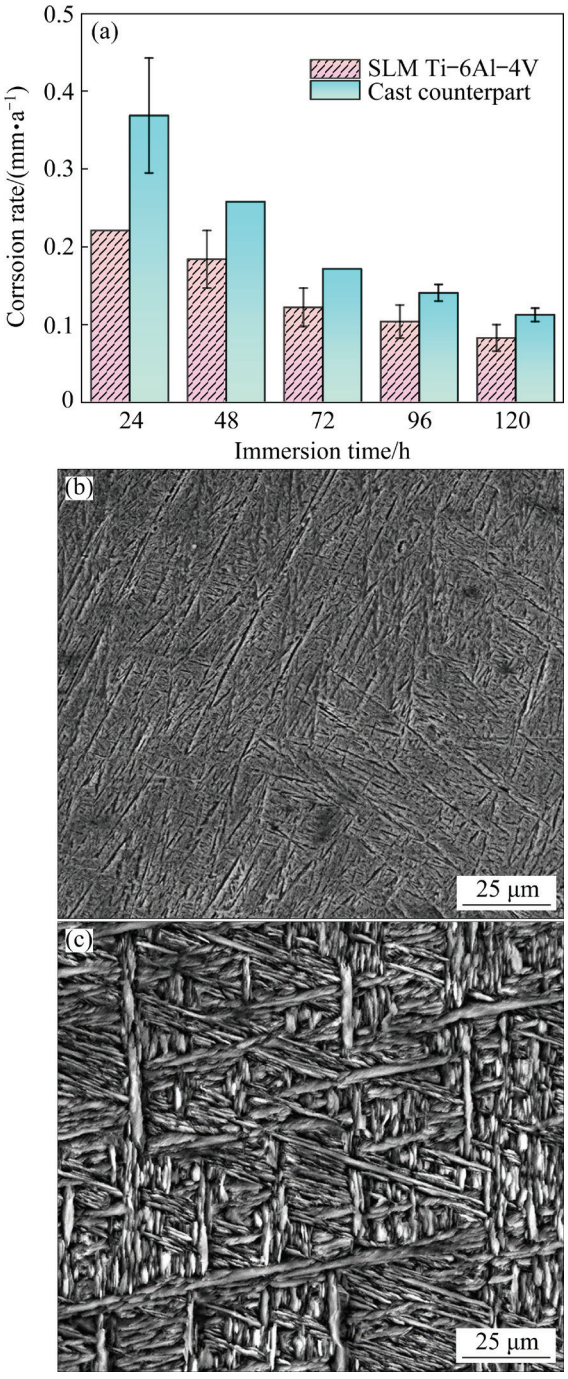

Fig. 5 Corrosion rate (a), and corrosion morphologies of SLM Ti−6Al−4V alloy (b) and cast counterpart (c) after immersing in 6 mol/L hot HNO_3 with oxidizing ions

120 h immersion. It can be seen that the corrosion rate is dependent on the time, with a high corrosion rate at beginning and then the gradually decreasing values of corrosion rate, which may be related to the formation and development of passive film in nitric acid. Furthermore, the surface morphologies of SLM Ti−6Al−4V alloy and the cast counterpart after 120 h immersion tests are shown in Figs. 5(b, c). It can be found that there is only a relatively slight corrosion on the surface of SLM Ti−6Al−4V alloy, while a severe corrosion surface is recorded for the cast counterpart. This indicates that the SLM Ti−6Al−4V alloy exhibits a higher resistance to corrosion in hot nitric acid media, which is consistent with the results of electrochemical analysis.

3.4 XPS analysis results

The XPS is conducted to determine the composition of passive film of both the SLM Ti−6Al−4V alloy and the cast counterpart formed in nitric acid containing oxidizing ions. And the spectra of Ti 2p, Al 2p and V 2p of these two alloys are obtained and presented in Fig. 6. Figures 6(a, b) show the Ti 2p spectra of two titanium alloys. It is apparent that the Ti 2p spectra exhibit four main peaks at about 458.6, 456.8, 464.2 and 462.0 eV corresponding to the TiO_2 (Ti $2p_{3/2}$), Ti_2O_3 (Ti $2p_{3/2}$), TiO_2 (Ti $2p_{1/2}$) and Ti_2O_3 (Ti $2p_{1/2}$), respectively [38,39]. Figures 6(c, d) display the Al 2p spectra, and there is only one component of Al_2O_3 which corresponds to the peak at 74.2 eV (Al $2p_{3/2}$) [40]. Moreover, the spectra of V 2p are also obtained, as shown in Figs. 6(e, f), which show a peak at 516.5 eV (V $2p_{3/2}$) corresponding to V_2O_4 based on relevant study [41]. Clearly, both SLM Ti−6Al−4V alloy and the cast counterpart have the same passive film composition (TiO_2, Ti_2O_3, Al_2O_3 and V_2O_4). Meanwhile, Figs. 6(g, h) show the XPS depth profiles of SLM Ti−6Al−4V alloy and the cast counterpart. It can be seen that the element concentration in the passive film shows a similar evolution trend for these two alloys. The content of Ti increases with the sputtering time, while that of V or Al decreases with the sputtering time. However, it can be found that the Ti content of SLM Ti−6Al−4V alloy is higher than that of the cast counterpart at the beginning of sputtering, which means that the content of Ti in the passive film of SLM Ti−6Al−4V alloy is higher than that of the cast counterpart.

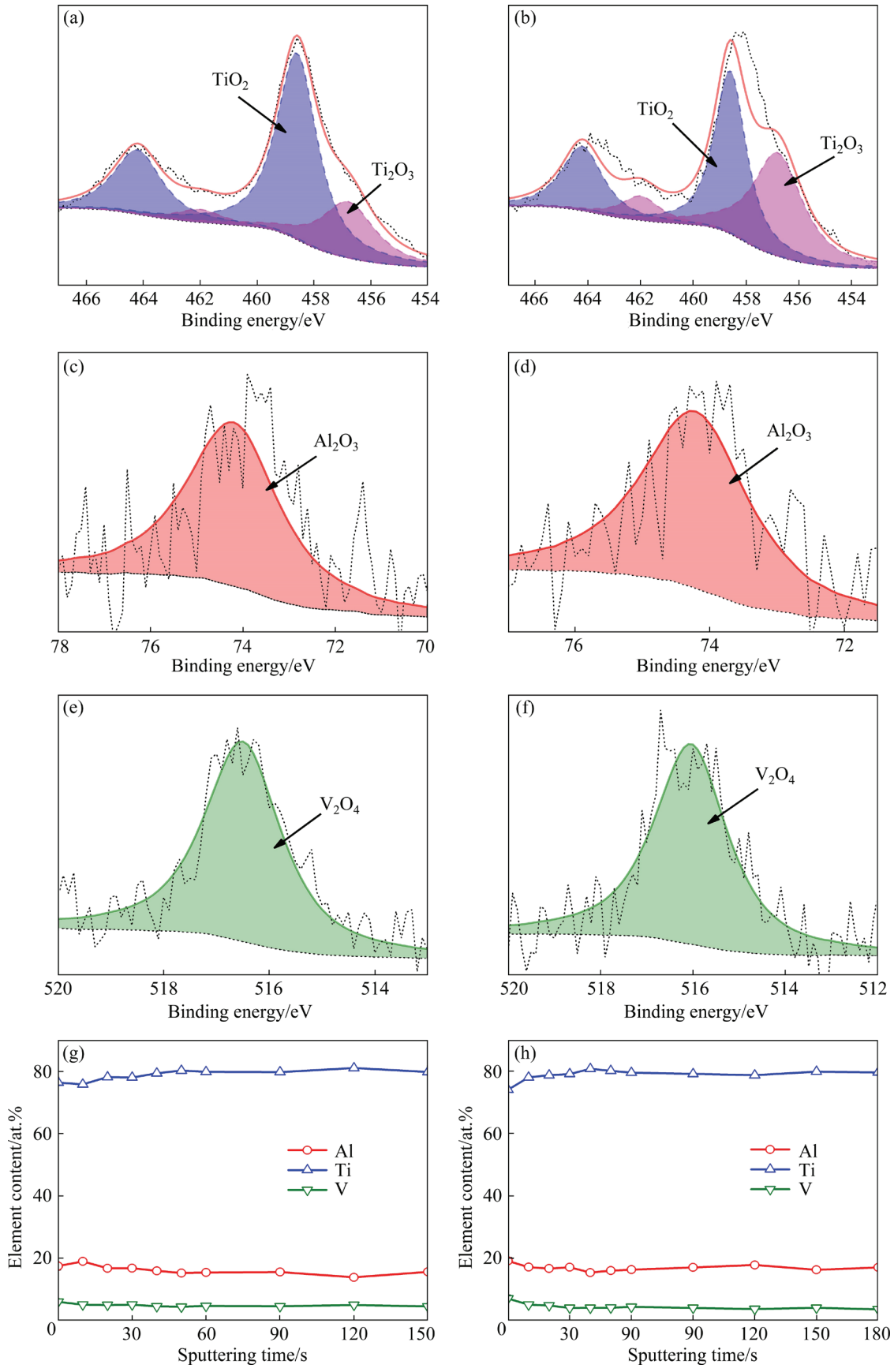

Fig. 6 XPS spectra of Ti 2p (a, b), Al 2p (c, d), V 2p (e, f), and depth profiles (g, h) for SLM Ti−6Al−4V alloy (a, c, e, g) and cast counterpart (b, d, f, h)

4 Discussion

4.1 Effect of microstructure and passive film characteristics on corrosion resistance of SLM Ti−6Al−4V alloy

From the results of the electrochemical measurements and corrosion mass loss, it is clear that SLM Ti−6Al−4V alloy shows a better corrosion resistance than the cast counterpart in nitric acid containing oxidizing ions. The better corrosion resistance of SLM Ti−6Al−4V alloy can be first attributed to its special microstructure. As described in Section 3.1, SLM Ti−6Al−4V alloy presents small grain size with the $\alpha'+\beta$ microstructure, while the cast counterpart displays large grain size with the $\alpha+\beta$ microstructure. On the one hand, the small grain size of SLM Ti−6Al−4V alloy has a considerable impact on its corrosion resistance. When considering the effect of grain size on corrosion, it has been suggested that the corrosion resistance of materials is improved with the decrease in grain size, since the surface with a high grain boundary density is prone to passivation [42,43]. Actually, many defects such as vacancies, exist at the grain boundaries which provide short diffusion channels for the atoms, thereby producing more active sites for the nucleation and growth of passive film [42,44]. Thus, the diffusion of atoms at grain boundaries is much faster than that in the grains. Accordingly, the small grain size of SLM Ti−6Al−4V alloy is conducive to its rapid formation of passive film in nitric acid, leading to a better passivation ability of SLM Ti−6Al−4V alloy. Besides, the α'-Ti phase in SLM Ti−6Al−4V alloy is in high energy state in comparison with α-Ti phase in the cast counterpart, which can also promote the passivation capacity of alloys in nitric acid. On the other hand, the better corrosion resistance of SLM Ti−6Al−4V alloy can also be related to its high content and uniform distribution of β-Ti phase. In the SLM fabricating process, the melt pool formed by the rapid melting of titanium alloy powder can solidify at a cooling rate of up to 10^4−10^8 K/s. Such high cooling rate can inhibit the transformation from β-Ti phase to α-Ti phase at high temperature, causing a high β-Ti phase content in SLM titanium alloy. Therefore, the SLM Ti−6Al−4V alloy presents a higher content of β-Ti phase compared with the cast counterpart. As given in Table 2, the content of β-Ti phase is 9.6% and 2.4% for SLM Ti−6Al−4V alloy and the cast counterpart, respectively. It has been reported that the β-Ti phase plays an important role in improving the corrosion resistance of titanium alloys [45−47]. The passive film formed on the β-Ti phase is more stable than that formed on the α-Ti phase, while the dissolution rate of β-Ti phase is lower than that of α-Ti phase. In addition, relevant investigation indicated that a higher content of β-Ti phase in titanium alloys can increase the resistance to charge transfer in double layer, thereby reducing the dissolution rate of titanium alloys [48]. Moreover, in this study, compared with the cast counterpart, uniformly distributed β-Ti phase in SLM Ti−6Al−4V alloy is observed, which can be also beneficial to the corrosion resistance of SLM alloy.

Furthermore, the electrochemical experiment results reveal that SLM Ti−6Al−4V has passive film with better properties, and it displays a lower J_{pass} compared with the cast counterpart. As mentioned previously, a higher Ti content in the passive film of SLM Ti−6Al−4V alloy is observed in comparison with the cast counterpart. Since Ti is the main protective element in the passive film, the high content of Ti in the passive film of SLM Ti−6Al−4V alloy can increase the protection ability of passive film, thereby improving its corrosion resistance. Meanwhile, Mott−Schottky tests and corrosion morphology show that a denser passive film with a low donor concentration is formed on SLM Ti−6Al−4V alloy compared with that on the cast counterpart, which confirms a better protection ability of passive film of SLM Ti−6Al−4V alloy. Moreover, in this study, a thicker passive film of SLM Ti−6Al−4V alloy is found according to the EIS analysis.

Considering all the aforementioned reasons, it is reasonable to conclude that the SLM Ti−6Al−4V alloy exhibits higher corrosion resistance than the cast counterpart due to its special microstructure with smaller grain size and higher content of β-Ti phase, which enhances the passivation ability of SLM alloys and promotes the formation of a high-quality passive film in nitric acid containing oxidizing ions.

4.2 Application prospect of SLM titanium alloys in reprocessing plant

To further illustrate the comprehensive

properties of SLM titanium alloys and clarify their application prospects in reprocessing plants, the SLM Ti−6Al−4V alloy is compared with the stainless steels and traditionally processed titanium alloys. By summarizing the obtained corrosion data, the mechanical and corrosion-resistant property diagram of titanium alloys and stainless steels is shown in Fig. 7 (The compositions of these materials are given in Table 6). It is clear that titanium alloys including SLM Ti−6Al−4V alloy show high tensile strength and superior corrosion resistance, while stainless steels display relatively low tensile strength and high corrosion rate. Specifically, with regard to stainless steels, the corrosion rates from high to low are 304L (0.68 mm/a), 310L (0.34 mm/a), 316L (0.29 mm/a) and H-Si steel (0.24 mm/a). And H-Si steel shows the lowest tensile strength of about 400 MPa, while other stainless steels display a high tensile strength of about 500 MPa. As for the titanium alloys, all of them present a low corrosion rate (<0.10 mm/a) in nitric acid containing oxidizing ions. And the tensile strength of these titanium alloys is much higher than that of stainless steels. It should be pointed out that the tensile strength of these titanium alloys shows great difference. For example, TA10 shows the lowest tensile strength of about 500 MPa, while Ti60 displays the highest tensile strength of about 1100 MPa.

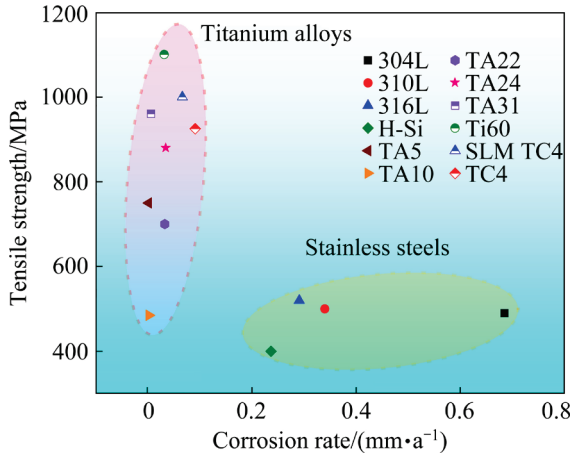

Fig. 7 Mechanical and corrosion-resistant property diagram of titanium alloys and stainless steels (The compositions of these materials are given in Table 6)

Table 6 Composition of materials shown in Fig. 7

Material	Composition
304L	Fe−18Cr−10Ni−1.6Mn−0.02C
310L	Fe−25Cr−20Ni−0.02C
316L	Fe−18Cr−12Ni−2Mo−0.02C
H-Si	Fe−18Cr−15Ni−3.8Si−0.01C
TA5	Ti−4Al−0.005B
TA10	Ti−0.3Mo−0.8Ni
TA22	Ti−3Al−1Mo−1Ni−1Zr
TA24	Ti−3Al−2Mo−2Zr
TA31	Ti−6Al−3Nb−2Zr−1Mo
Ti60	Ti−5.8Al−4.8Sn−2Zr−1Mo−0.35Si−0.85Nd
TC4	Ti−6Al−4V

Importantly, SLM titanium alloys as well as traditional titanium alloys present superior comprehensive properties compared with stainless steels. However, it should be noted that the cost of titanium alloys is much higher than that of stainless steels, and the formability of titanium alloys is worse than that of stainless steels. Therefore, considering the cost and formability, stainless steels are widely used as the structure materials for some normal reprocessing environments where corrosion rate is not strictly required. However, under extremely harsh corrosive environment, stainless steels will encounter IGC and dissolve at a high corrosion rate. Thus, for this case, titanium alloys with better corrosion resistance should be applied to ensuring the operation safety of reprocessing plant. For SLM Ti−6Al−4V alloy, it shows superior comprehensive properties with high tensile strength (about 1000 MPa) and relatively low corrosion rate (within 0.10 mm/a) compared with stainless steels. Particularly, on the basis of SLM technology, the titanium alloy parts used in reprocessing with complex configuration and high precision can be efficiently produced at a relatively low cost. Hence, SLM titanium alloys have a prospective application in spent fuel reprocessing in the view of their good formability, low cost and superior comprehensive properties.

5 Conclusions

(1) The electrochemical measurements and corrosion loss measurements demonstrated that SLM Ti−6Al−4V alloy displays better corrosion resistance than the cast counterpart in nitric acid with oxidizing ions. Further analysis shows that a thicker and denser passive film is formed on SLM Ti−6Al−4V alloy with a low donor content

compared with that on the cast counterpart, which enhances the protection ability of SLM alloy in hot nitric acid media.

(2) Microstructure analysis shows that SLM Ti−6Al−4V alloy presents the $\alpha'+\beta$ microstructure with smaller grain size in comparison to the cast counterpart. The smaller grain size with a higher grain boundary density is conducive to the rapid formation of passive film in nitric acid, thus improving the passivation ability of SLM alloy. Moreover, compared with the cast counterpart, a higher content of β-Ti phase with uniform distribution is observed in SLM Ti−6Al−4V alloy, which is also favorable for its corrosion resistance.

(3) SLM Ti−6Al−4V alloy exhibits a higher tensile strength (~1000 MPa) and a lower corrosion rate (<0.10 mm/a) compared with traditional stainless steels. Meanwhile, on the basis of SLM technology, the titanium alloy parts used in reprocessing with complex configuration and high precision can be efficiently produced at a relatively low cost, displaying promising application prospect in spent fuel reprocessing field.

CRediT authorship contribution statement

Zheng LIU: Investigation, Formal analysis; **Lian-min ZHANG:** Conceptualization, Writing – Review and editing, Supervision; **De-chun REN**, **Ai-li MA** and **Hai-bin JI:** Formal analysis, Investigation; **Yu-gui ZHENG:** Writing – Review and editing, Supervision.

Declaration of competing interest

The authors declare that they have no known competing financial interests or personal relationships that could have appeared to influence the work reported in this paper.

Acknowledgments

This work was supported by IMR Innovation Fund, China (No. 2023-PY03), and the National Natural Science Foundation of China (No. 52101105).

References

[1] BALDEV R, MUDALI U K. Materials development and corrosion problems in nuclear fuel reprocessing plants [J]. Progress in Nuclear Energy, 2006, 48: 283−313.

[2] NASH K L, NILSSON M. Introduction to the reprocessing and recycling of spent nuclear fuels, reprocessing & recycling of spent nuclear fuel [M]. Woodhead Publishing Series in Energy, 2015.

[3] NINGSHEN S, MUDALI U K, RAMYA S, RAJ B. Corrosion behavior of AISI type 304L stainless steel in nitric acid media containing oxidizing species [J]. Corrosion Science, 2011, 53: 64−70.

[4] NINGSHEN S, MUDALI U K, AMARENDRA G, BALDEV R. Corrosion assessment of nitric acid grade austenitic stainless steels [J]. Corrosion Science, 2009, 51: 322−329.

[5] FAUVET P, BALBAUD F, ROBIN R, TRAN Q T, MUGENIER A, ESPINOUX D. Corrosion mechanisms of austenitic stainless steels in nitric media used in reprocessing plants [J]. Journal of Nuclear Materials, 2008, 375: 52−64.

[6] GWINNER B, AUROY M, BALBAUD F, FAUVET P, LARABI N, LAGHOUTARIS P, ROBIN R. Towards a reliable determination of the intergranular corrosion rate of austenitic stainless steel in oxidizing media [J]. Corrosion Science, 2016, 107: 60−75.

[7] IOKA I, SUZUKI J, MOTOKA T, KIUCHI K, NAKAYAMA J. Correlation between intergranular corrosion and impurities of extra high purity austenitic stainless steels [J]. Journal of Power and Energy Systems, 2010, 4: 105−112.

[8] NINGSHEN S, SAKAIRI M, SUZUKI K, OKUNO T. Corrosion performance and surface analysis of Ti−Ni−Pd−Ru−Cr alloy in nitric acid solution [J]. Corrosion Science, 2015, 91: 120−128.

[9] NINGSHEN S, KAMACHI U, MUKHERJEE P, BARAT P, BALDEV R. Oxygen ion irradiation effect on corrosion behavior of titanium in nitric acid medium [J]. Journal of Nuclear Materials, 2011, 408: 1−6.

[10] DEBROY T, WEI H L, ZUBACK J S, MUKHERJEE T, ELMER J W, MILEWSKI J O, BEESE A M, WILSON-HEID A, DE A, ZHANG W. Additive manufacturing of metallic components – Process, structure and properties [J]. Progress in Materials Science, 2018, 92: 112−224.

[11] OSMAN H, LIU L. Additive manufacturing of high-entropy alloy composites: A review [J]. Transactions of Nonferrous Metals Society of China, 2023, 33: 1−24.

[12] SU Xu-bin, YANG Yong-qiang, YU Peng, SUN Jian-feng, Development of porous medical implant scaffolds via laser additive manufacturing [J]. Transactions of Nonferrous Metals Society of China, 2012, 22(Suppl.): 181−187.

[13] FRAZIER W E. Metal additive manufacturing: A review [J]. Journal of Materials Engineering and Performance, 2014, 23: 1917−1928.

[14] BARTOLOMEU F, BUCIUMEANU M, PINTO E, ALVES N, SILVA F S, CARVALHO O, MIRANDA G. Wear behavior of Ti6Al4V biomedical alloys processed by selective laser melting, hot pressing and conventional casting [J]. Transactions of Nonferrous Metals Society of China, 2017, 27: 829−838.

[15] GORSE S, HUTCHINSON C, GOUNE M, BANERJEE R. Additive manufacturing of metals: A brief review of the characteristic microstructures and properties of steels, Ti−6Al−4V and high-entropy alloys [J]. Science and Technology of Advanced Materials, 2017, 18: 584−610.

[16] GU Dong-dong, WANG Hong-qiao, ZHANG Guo-quan, Selective laser melting additive manufacturing of Ti-based

nanocomposites: The role of nanopowder [J]. Metallurgical and Materials Transactions A, 2014, 45: 464−476.

[17] ATTAR H, CALIN M, ZHANG L C, SCUDINO S, ECKERT J. Manufacture by selective laser melting and mechanical behavior of commercially pure titanium [J]. Materials Science and Engineering A, 2014, 593: 170−177.

[18] ZHANG L C, KLEMM D, ECKERT J, HAO Y L, SERCOMBE T B. Manufacture by selective laser melting and mechanical behavior of a biomedical Ti−24Nb−4Zr−8Sn alloy [J]. Scripta Materialia, 2011, 65: 21−24.

[19] GU D D, HAGEDORN Y C, MEINERS W, MENG G B, BATISTA R J S, WISSENBACH K, POPRAWE R. Densification behavior, microstructure evolution, and wear performance of selective laser melting processed commercially pure titanium [J]. Acta Materialia, 2012, 60: 3849−3860.

[20] SALLICA E, JARDINI A L, FOGAGNOLO J B. Microstructure and mechanical behavior of porous Ti−6Al−4V parts obtained by selective laser melting [J]. Journal of the Mechanical Behavior of Biomedical Materials, 2013, 26: 98−108.

[21] ZHANG Qi, LIANG Zheng-long, CAO Miao, LIU Zi-fan, ZHANG An-feng, LU Bing-heng. Microstructure and mechanical properties of Ti6Al4V alloy prepared by selective laser melting combined with precision forging [J]. Transactions of Nonferrous Metals Society of China, 2017, 27: 1036−1042.

[22] PAL S, FINSGAR M, BONCINA T, LOJEN G, BRAJLIH T, DRSTVENSEK L. Effect of surface powder particles and morphologies on corrosion of Ti−6Al−4 V fabricated with different energy densities in selective laser melting [J]. Materials & Design, 2021, 211: 110184.

[23] HAMZA H M, DEEN K M, HAIDER W. Microstructural examination and corrosion behavior of selective laser melted and conventionally manufactured Ti6Al4V for dental applications [J]. Materials Science and Engineering C, 2020, 113: 110980.

[24] JU Jiang, LI Jing-jing, JIANG Min, LI Meng-ya, YANG Li-xiang, WANG Kai-ming, YANG Chao, KANG Mao-dong, WANG Jun. Microstructure and electrochemical corrosion behavior of selective laser melted Ti−6Al−4V alloy in simulated artificial saliva [J]. Transactions of Nonferrous Metals Society of China, 2021, 31: 167−177.

[25] SUN Sheng-xun, ZHANG Lian-min, Ma Ai-li, DANIEL E F, ZHANG Chun-zhi, ZHENG Yu-gui. Comparison of the three-phase corrosion behavior of SiN and 304L stainless steels in 6 M nitric acid solution at different temperatures [J]. Metals, 2022, 12: 922.

[26] VRANCKEN B, THIJS L, KRUTH J P, HUMBEECK J V. Heat treatment of Ti6Al4V produced by selective laser melting: Microstructure and mechanical properties [J]. Journal of Alloys and Compounds, 2012, 41: 177−185.

[27] THIJS L, VERHAEGHE F, CRAEGHS T, HUMBEECK J V, KRUTH J P. A study of the microstructural evolution during selective laser melting of Ti−6Al−4V [J]. Acta Materialia, 2010, 58: 3303−3312.

[28] FACCHINI L, MAGALINI E, ROBOTTI P, MOLINARI A, HOGES S, WISSENBACH K. Ductility of a Ti−6Al−4V alloy produced by selective laser melting of prealloyed powders [J]. Rapid Prototyping Journal, 2010, 16: 450−459.

[29] SING S L, YEONG W Y, WIRIA F E. Selective laser melting of titanium alloy with 50 wt.% tantalum: microstructure and mechanical properties [J]. Journal of Alloys and Compounds, 2016, 660: 461−470.

[30] HAGHIGHI S E, LU H B. JIAN G Y, HABIBI D, ZHANG L C. Effect of α'' martensite on the microstructure and mechanical properties of beta-type Ti−Fe−Ta alloys [J]. Materials & Design, 2015, 76: 47−54.

[31] HAGHIGHI S E, LIU Yu-jing, CAO Guang-hui, ZHANG Lai-chang. Phase transition, microstructural evolution and mechanical properties of Ti−Nb−Fe alloys induced by Fe addition [J]. Materials & Design, 2016, 97: 279−286.

[32] SICSIC D, CELERIER F B, TRIBOLLET B. Mechanism of nitric acid reduction and kinetic modelling [J]. European Journal of Inorganic Chemistry, 2014, 2014: 6174−6184.

[33] FAUVET P. 19-Corrosion issues in nuclear fuel reprocessing plants [M]. Woodhead Publishing Series in Energy, 2012.

[34] LIU Z, ZHANG L M, CHEN W Q, MA A L, ZHENG Y, YAN W, LI Y F, DANIEL E F, SHAN Y Y, ZHENG Y G. Effect of oxidizing ions on the corrosion behavior of SiN stainless steel in high-temperature nitric acid solution [J]. Electrochimica Acta, 2023, 442: 141917.

[35] HSU C H, MANSFELD F. Technical note: Concerning the conversion of the constant phase element parameter Y_0 into a capacitance [J]. Corrosion, 2001, 57: 747−748.

[36] ZHANG L M, ZHANG S D, MA A L, UMOH A J. HU H X, ZHENG Y G, YANG B J, WANG J Q. Influence of cerium content on the corrosion behavior of Al−Co−Ce amorphous alloys in 0.6 mol/L NaCl solution [J]. Journal of Materials Science & Technology, 2019, 35: 1378−1387.

[37] LI Z X, ZHANG L M, Ma A L, HU J X, ZHANG S, DANIEL E F, ZHENG Y G. Comparative study on the cavitation erosion behavior of two different rolling surfaces on 304 stainless steel [J]. Tribology International, 2021, 159: 106994.

[38] WANG Z B, HU H X, LIU C B, ZHENG, Y G. The effect of fluoride ions on the corrosion behavior of pure titanium in 0.05 mol/L sulfuric acid [J]. Electrochimica Acta, 2014, 135: 526−535.

[39] MILOSEV I, KOSEC T, STREHBLOW H H. XPS and EIS study of the passive film formed on orthopaedic Ti−6Al−7Nb alloy in Hank's physiological solution [J]. Electrochimica Acta, 2008, 53: 3547−3558.

[40] MILOSEV I, HUKOVIC M M, STREHBLOW H H. Passive film on orthopaedic TiAlV alloy formed in physiological solution investigated by X-ray photoelectron spectroscopy [J]. Biomaterials, 2000, 21: 2103−2113.

[41] MINYAEV A I, DENISOV I A, SOROKO V E, KONOVALOV V A. Study of solid-phase transformations in vanadium systems [J]. Zhurnal Pikladnoi Khimii, 1986, 59: 339−343. (in Russian)

[42] RALSTON K D, BIRBILIS N, DAVIES C H J. Revealing the relationship between grain size and corrosion rate of metals [J]. Scripta Materialia, 2010, 63: 1201−1204.

[43] KUS E, LEE Z, NUTT S, MANSFELD F. A comparison of the corrosion behavior of nanocrystalline and conventional Al 5083 samples [J]. Corrosion, 2006, 62: 152−161.

[44] BASAK C B, SENGUPTA A K. Development of a FDM

based code to determine the 3-D size distribution of homogeneously dispersed spherical second phase from microstructure: A case study on nodular cast iron [J]. Scripta Materialia, 2004, 51: 255−260.

[45] CHEN Jhen-rong, TSAI Wen-ta. In situ corrosion monitoring of Ti−6Al−4V alloy in H_2SO_4/HCl mixed solution using electrochemical AFM [J]. Electrochimica Acta, 2011, 56: 1746−1751.

[46] DAI Nian-wei, ZHANG Lai-chang, ZHANG Jun-xi, CHEN Qi-meng, WU Mao-liang. Corrosion behavior of selective laser melted Ti−6Al−4V alloy in NaCl solution [J]. Corrosion Science, 2016, 102: 484−489.

[47] DAI Nian-wei, ZHANG Lai-chang, ZHANG Jun-xi, ZHANG Xin, NI Qing-zhao, CHEN Yang, WU Mao-liang, YANG Chao. Distinction in corrosion resistance of selective laser melted Ti−6Al−4V alloy on different planes [J]. Corrosion Science, 2016, 111: 703−710.

[48] BAI Yun, GAI Xin, LI Shu-jun, ZHANG Lai-chang, LIU Yu-jing, HAO Yu-lin, ZHANG Xing, YANG Rui, CAO Yong-bo. Improved corrosion behavior of electron beam melted Ti−6Al−4V alloy in phosphate buffered saline [J]. Corrosion Science, 2017, 123: 289−296.

选区激光熔化 Ti−6Al−4V 合金在模拟乏燃料后处理环境中的腐蚀行为

刘 政[1,2]，张连民[1]，任德春[3]，马爱利[1]，吉海宾[3]，郑玉贵[1]

1. 中国科学院 金属研究所 中科院核用材料与安全评价重点实验室，沈阳 110016；
2. 中国科学技术大学 材料科学与工程学院，沈阳 110016；
3. 中国科学院 金属研究所 师昌绪先进材料创新中心，沈阳 110016

摘 要：研究选区激光熔化(SLM)制备的 Ti−6Al−4V 合金在乏燃料后处理环境中的腐蚀行为。借助光学显微镜、X 射线衍射、扫描电子显微镜、电子背散射衍射以及电化学测试等手段研究 SLM Ti−6Al−4V 合金的显微组织及耐蚀性。结果表明，相较于铸造合金，SLM Ti−6Al−4V 合金在含氧化性离子的 6 mol/L 热硝酸溶液中的耐腐蚀性更好。进一步分析表明，SLM Ti−6Al−4V 合金具有 α'+β 的微观结构，β-Ti 相含量较高且分布均匀，同时其晶粒尺寸较小、晶界密度较高，这种微观结构可提高其在含氧化性离子的硝酸中的钝化能力以及耐腐蚀性。SLM Ti−6Al−4V 合金有望在乏燃料后处理过程中得到广泛应用。

关键词：乏燃料后处理；选区激光熔化；Ti−6Al−4V 合金；腐蚀行为；钝化性能

(Edited by Bing YANG)